Structural evolution of short-range order in CrCoNi and MnCoNi medium-entropy alloys

Masataka Mizuno [*] and Hideki Araki

Division of Materials and Manufacturing Science, Graduate School of Engineering, Osaka University,
2-1 Yamadaoka, Suita, Osaka 565-0871, Japan

Short-range order (SRO) is predicted in Cr- or Mn-containing face-centered-cubic (fcc) concentrated solid-solution alloys. One possible reason for SRO is the magnetic frustration of parallel spin pairs. The presence of SRO is expected to improve physical and mechanical properties. However, changes in atomic and magnetic structures induced by SRO are not clear. In the current study, the SRO in fcc CrCoNi and MnCoNi medium-entropy alloys was investigated using first-principles-based Monte Carlo simulations. In the initial stage of SRO, $L1_2$-type ordering occurs by the formation of second nearest-neighbor (NN) Cr-Cr or Mn-Mn bonds with decreasing first NN Cr-Cr or Mn-Mn bonds. These SROs originate from the energy gain caused by the decrease in the number of Cr-Cr or Mn-Mn parallel pairs. After the initial stage of SRO in MnCoNi, Mn-rich and Mn-poor layers were formed along one of the $\langle 100 \rangle$ directions, leading to $L1_0$-type ordering. Antiparallel Mn-Mn pairs were formed in the Mn-rich layers. In contrast, in CrCoNi, the occupation of Cr atoms on the $\{110\}$ planes in every three layers was promoted after the initial stage of SRO. The difference in the SRO after $L1_2$-type ordering was considered to arise from the lower magnetic moment of the Cr atoms in CrCoNi compared with that of the Mn atoms in MnCoNi. The energy gain owing to the formation of SRO suggests that MnCoNi possesses a larger driving force for SRO formation than CrCoNi.

I. INTRODUCTION

The chemical short-range order (SRO) in a face-centered-cubic (fcc) structure has recently attracted considerable attention in Cr-containing medium-entropy alloys (MEAs) and high-entropy alloys (HEAs), wherein the Cr atoms tend to form antiparallel spin pairs with neighboring atoms [1–4]. In an fcc structure, parallel spin pairs are inevitably formed because the triangles consist of three nearest-neighbor (NN) bonds. In an fcc CrMnFeCoNi high-entropy alloy [5], an antiferromagnetic arrangement is favored in the vicinity of Cr atoms, even in the ferromagnetic state [6]. In addition, antiparallel pairs are observed near the Mn atoms in the ferromagnetic state. Therefore, in Cr- or Mn-containing fcc concentrated solid solutions, SRO is expected to decrease the magnetic frustration of parallel pairs.

Using Monte Carlo (MC) simulations combined with first-principles calculations, Tamm *et al.* predicted that SRO involves a decrease in the number of Cr-Cr pairs together with an increase in the number of Ni-Cr and Cr-Co pairs in CrCoNi and CrFeCoNi alloys [1]. Since then, several experimental [7–15] and theoretical [1,3,4,16–18] studies have focused on SRO in CrCoNi alloys. For example, an increase in the number of Ni-Cr and Cr-Co pairs was experimentally suggested using extended x-ray absorption analysis [7]. The increase in the electrical resistivity suggesting the formation of SRO in CrCoNi was reported [14,15]. Regarding mechanical properties, Zhang *et al.* [8] reported the hardening caused

by the formation of SRO in CrCoNi, while several other groups reported that no significant changes in the mechanical properties were observed by the formation of SRO in CrCoNi [9,10,14,15]. In addition, to quantitatively evaluate the degree of SRO, the Warren-Cowley (WC) parameter [19] was used for the first and second NN bonds. It was found that in the case of CrCoNi, the WC parameters of the first NN and second NN Cr-Cr bonds increased and decreased, respectively [1]. This suggests that the corner sites are preferentially occupied by Cr atoms to avoid the formation of first NN Cr-Cr bonds, which leads to $L1_2$-type ordering. However, if the face-centered sites on one of the $\{100\}$ planes are also occupied by Cr atoms, the atomic arrangement of the SRO can be regarded as $L1_0$-type ordering, wherein the Cr-rich and Cr-poor layers are stacked alternately along one of the $\langle 100 \rangle$ directions. Therefore, to determine the ordering type of SRO, the change in atomic concentration along a specific direction must be examined. If an SRO evolves well, it can be recognized by visualizing the three-dimensional arrangement of atoms. In this context, Du *et al.* found two types of superlattices, namely Cr/CoNi $\{100\}$ and Cr/CoNi $\{110\}$, using a large-scale MC simulation with a neural network potential [17]. A Cr/CoNi $\{110\}$ superlattice was also observed by Ghosh *et al.* and assigned to MoPt$_2$-type ordering [18]. Subsequently, the energy difference between $L1_2$-type ordering and MoPt$_2$-type ordering was discussed. Furthermore, in their study on the linear response theory, Woodgate *et al.* [4] found that a MoPt$_2$-like order was favored in the magnetically ordered state, whereas an $L1_2$-like order was favored in the paramagnetic state in CrCoNi. However, nonmagnetic density function theory (DFT) calculations by Gosh *et al.* [18] also predicted the same type of ordering,

──────────
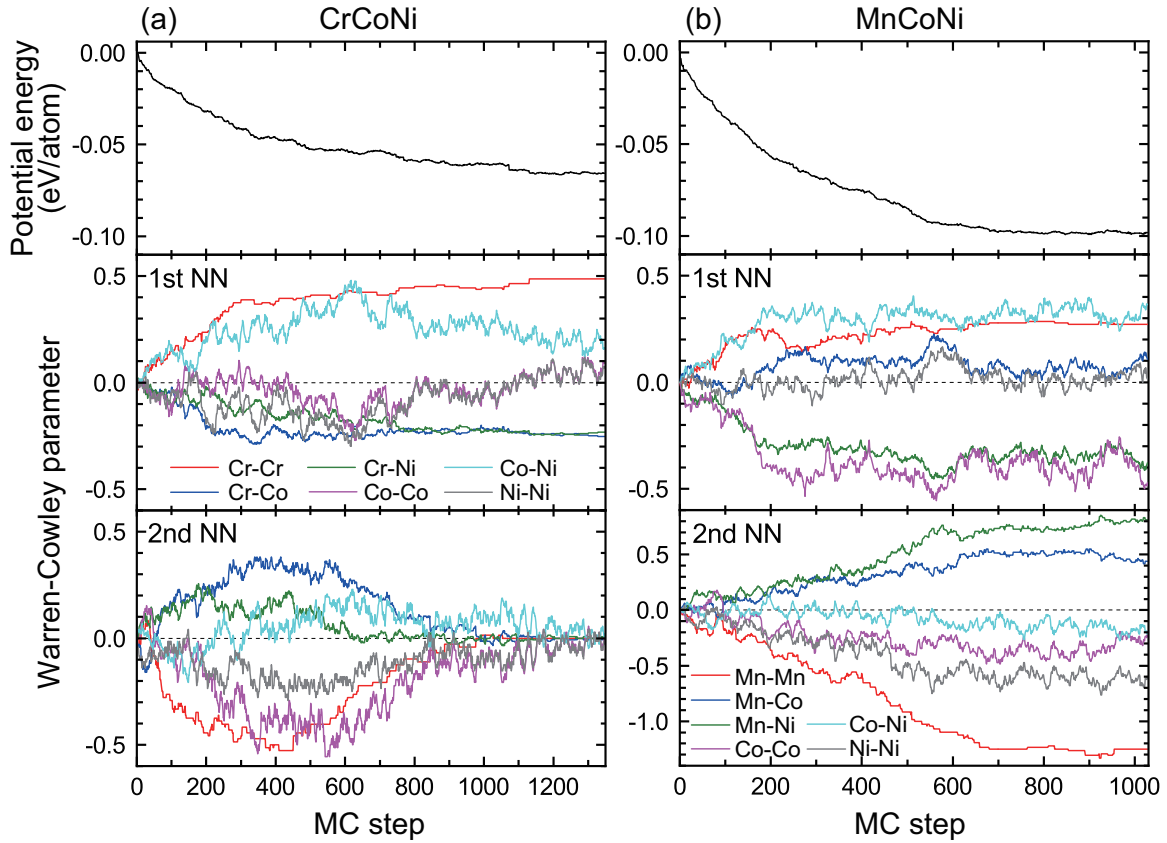[*]Corresponding author: mizuno@mat.eng.osaka-u.ac.jp

FIG. 1. Change in the potential energy and Warren-Cowley parameters for the first NN and second NN pairs during the MC simulations in (a) CrCoNi and (b) MnCoNi.

which suggests that the magnetism is not the driving force in determining the ground state in CrCoNi. Therefore, the contribution of the magnetic structure to the formation of $MoPt_2$-type ordering remains unclear since the evolution of $MoPt_2$-type ordering in CrCoNi has yet to be confirmed using first-principles calculations. One possible reason for this is the size of the supercells used in the MC simulations. In a supercell composed of 108 lattice sites with an fcc structure ($3 \times 3 \times 3$ unit cell), such as those used in previous works [1,3], a second NN bond was formed between the second NN atoms across the cell boundary, thereby contributing to the stability of the $L1_2$-type ordering. Thus, to clarify the difference in stability between $L1_2$-type and $MoPt_2$-type ordering, a larger supercell is required.

In previous works, the $L1_2$-type ordering was experimentally examined using atom probe tomography [10], while the Cr-enriched {113} planes in CrCoNi (similar to $MoPt_2$-type ordering) were observed using aberration-corrected transmission electron microscopy [11]. More recently, Umemoto *et al.* carried out neutron scattering experiments on MnCoNi and CrCoNi alloys [20]. The obtained neutron scattering profiles demonstrated the coexistence of the tetragonal long-range ordered phase ($L1_0$) and the short-range ordered phase in the MnCoNi samples, while no significant signals corresponding to short- or long-range ordering were observed in the CrCoNi samples. These results therefore indicate the requirement for theoretical approaches to clarify the origin of SRO in

MnCoNi. Although Mn atoms are known to occupy both the corner and face-centered sites in CrMnFeCoNi during MC simulations [21], no theoretical studies have been carried out on SRO in MnCoNi to support $L1_0$-type ordering.

Thus, in the current study, first-principles-based MC simulations are performed for fcc CrCoNi and MnCoNi MEAs to investigate the changes in their atomic and magnetic structures due to the formation of SRO. The importance of the magnetic moments of the Cr and Mn atoms is also highlighted in terms of the formation of SRO. Furthermore, the formation of $L1_0$-type ordering in MnCoNi is predicted, wherein the Mn-rich and Mn-poor planes are stacked alternately along one of the $\langle 100 \rangle$ directions.

II. COMPUTATIONAL METHOD

To calculate the energies of the ideal solid solutions of CrCoNi and MnCoNi, a supercell composed of 216 lattice sites and with an fcc structure ($6 \times 6 \times 6$ primitive cells) was employed. A disordered arrangement was constructed using the special-quasi-random structure (SQS) approach [22]. In a perfectly random AB alloy, the probability of finding a B atom on the jth nearest-neighbor shell of an A atom, defined as $P_{A\text{-}B}(j)$, should be equal to the concentration of B (x_B). Thus, the Warren-Cowley parameter [19], expressed as $\alpha^j_{A-B} = 1 - P_{A\text{-}B}(j)/x_B$, should be close to zero in a disordered model. Thus, the atomic configurations were
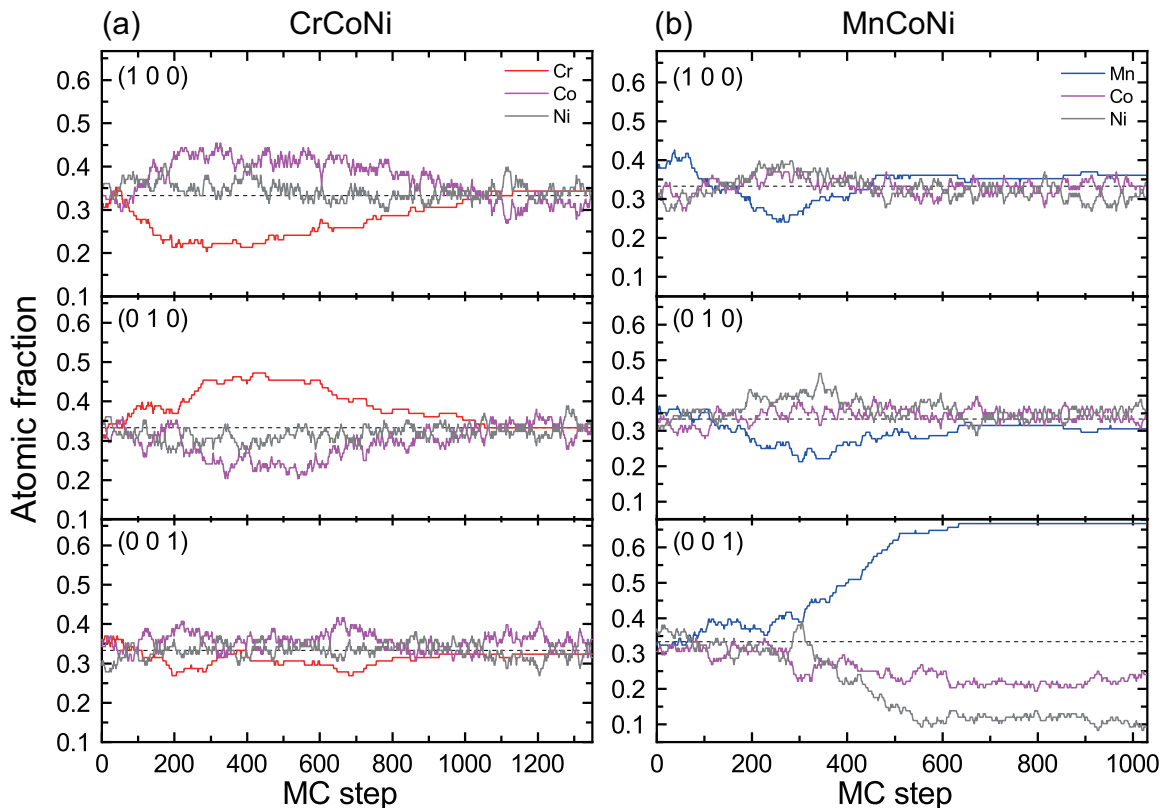
FIG. 2. Changes in the average concentrations of the various elements in pairs of (100), (010), and (001) planes during the MC simulations in (a) CrCoNi and (b) MnCoNi.

determined to set the Warren-Cowley parameter such that the shells up to the seventh nearest neighbor (NN) were close to zero. Positive values of $\alpha_{A\text{-}B}^{j}$ show a decrease in the number of jth NN A-B pairs, while negative values correspond to the opposite case. To examine chemical SRO, first-principles-based MC simulations were performed at 300 K, and Metropolis-Hastings sampling was employed to determine the acceptance probability of the position swap [23]. To calculate the energy during the MC simulations, the Vienna *ab initio* simulation package (VASP) [24,25] was employed with the Perdew-Burke-Ernzerhof (PBE) generalized gradient approximation [26]. The potentials used were based on the projector augmented wave (PAW) method [27,28]. Structural relaxation of the atoms was continued until the total energy change was reduced to <0.001 eV. To simulate the paramagnetic state, the up and down spins were distributed using the binary SQS model for the initial magnetic moment of the paramagnetic state prior to carrying out the MC simulations [6]. A kinetic energy cutoff of 350 eV and gamma point ($1\times1\times1$) mesh were used during the MC simulations. The results of evaluations of kinetic energy cutoff and k mesh are listed in Table S1 in the Supplemental Material [29].

III. RESULTS

A. Warren-Cowley parameter

Figure 1 shows the changes in the potential energy and the WC parameters for the first and second NN pairs during the MC simulations carried out for CrCoN and MnCoNi. No significant change was observed in the potential energy and the WC parameters near the end of the MC simulations both in CrCoNi and MnCoNi, which suggests that the MC simulations reached the equilibrium state in CrCoNi and MnCoNi. The enlarged view of the potential energy near the end of MC simulations is shown in Fig. S1 in the Supplemental Material [29]. The decrease in the potential energy of CrCoNi was approximately half of that of MnCoNi. Similar trends were observed for the Cr-Cr bonds in CrCoNi and the Mn-Mn bonds in MnCoNi up to 400 MC steps, wherein the WC parameter of the first NN pair increased, but that of the second NN pair decreased, indicating that the second NN pairs were formed by decreasing the number of first NN pairs. However, significant differences were observed for the two alloys in terms of the variation in the WC parameter of the second NN pairs after 400 MC steps. More specifically, in MnCoNi, the WC parameter of the second NN Mn-Mn pair decreased gradually during the MC simulation, while in CrCoNi, the WC parameter of the second NN Cr-Cr pair decreased during the initial 450 steps and then began to increase again. These results indicate that the second NN Cr-Cr bonds formed during the MC simulation of up to 450 steps are broken again. In CrCoNi, the other WC parameters of the second NN pairs also began to increase or decrease toward 0.

A common feature observed in both CrCoNi and MnCoNi is the increase in the WC parameter of the first NN Co-Ni pairs. As discussed below, in the Cr-poor layers of CrCoNi and the Mn-poor layers of MnCoNi, the Co and Ni atoms
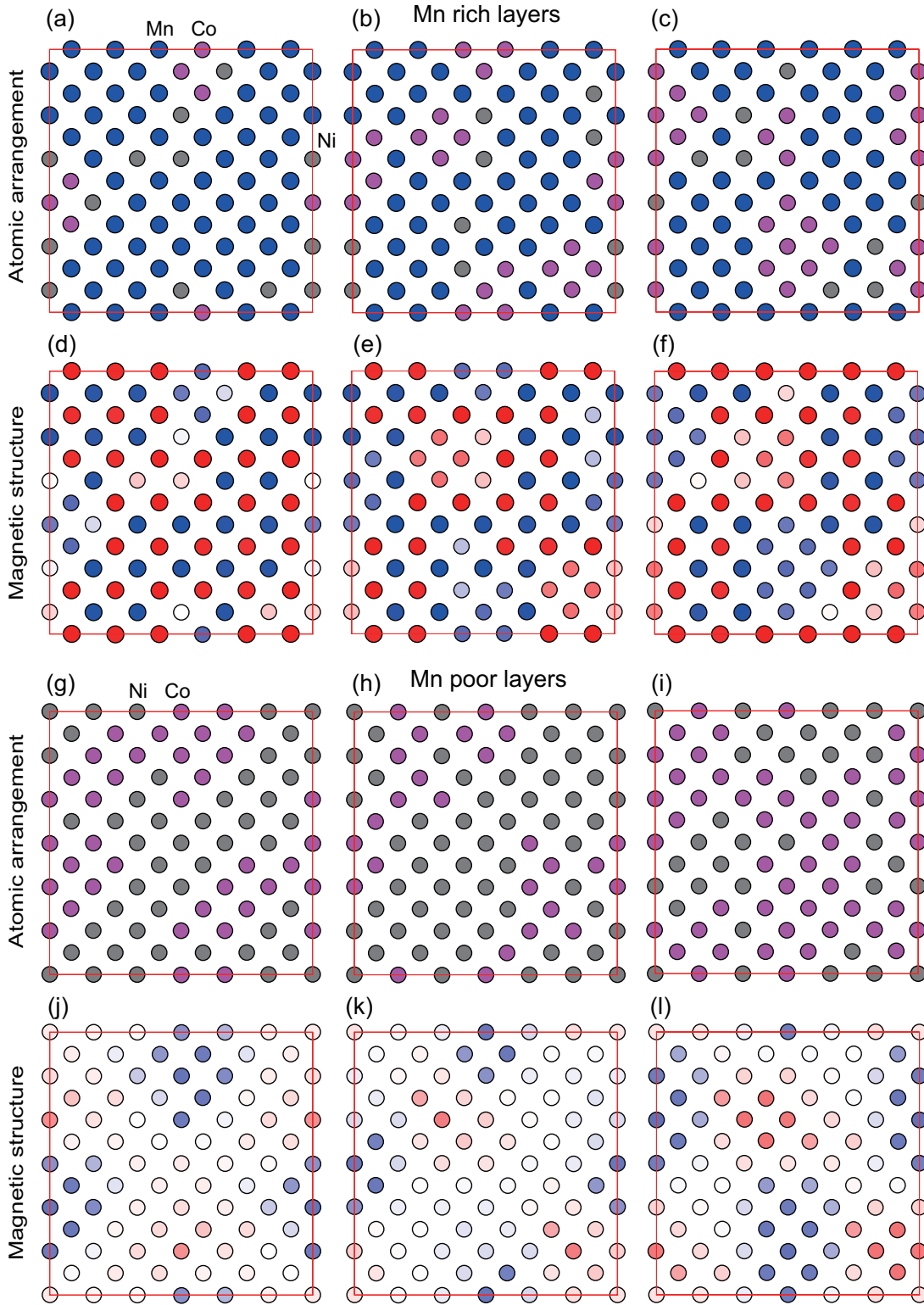
FIG. 3. Atomic structures in the (a)–(c) Mn-rich and in the (g)–(i) Mn-poor layers, along with the magnetic structures in the (d)–(f) Mn-rich and (j)–(l) Mn-poor layers of MoCoNi after 904 MC steps. The red and blue shadings in parts (d)–(f) and (j)–(l) represent the magnitudes of the magnetic moments normalized by $3.0\mu_B$ for the spin-up and spin-down states, respectively.

tend to form Co and Ni clusters, respectively. Therefore, the number of first NN Co-Ni pairs decreased during the MC simulations. The formation of Co clusters was observed as an increase in the WC parameters of the first NN Co-Co pairs in

MnCoNi. However, the WC parameters of the other first NN pairs in CrCoNi were close to zero. This difference arises from the formation of Co clusters in the Mn-rich layers in MnCoNi, as described below.
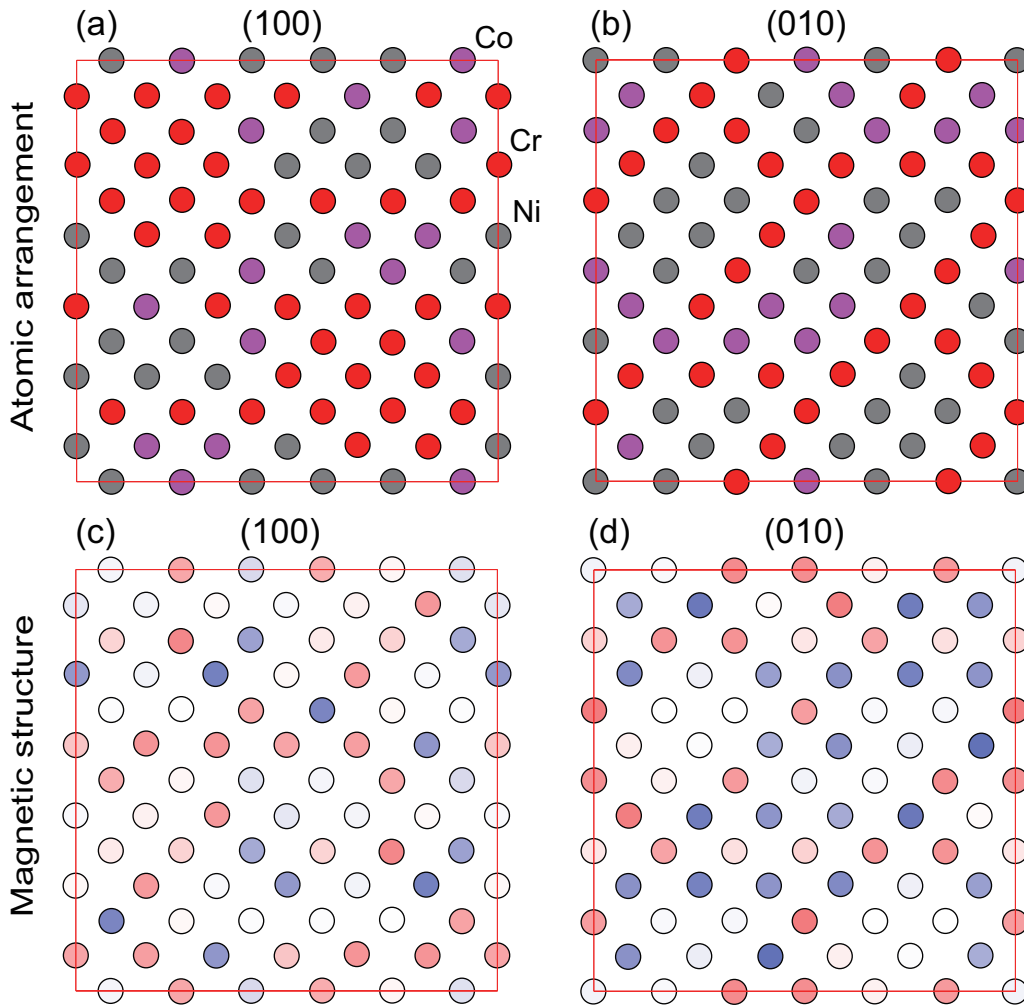
FIG. 4. Atomic structures in one of the (a) (100) and (c) (010) planes, along with the magnetic structures in one of the (b) (100) and (d) (010) planes of CrCoNi after 410 MC steps. The red and blue shadings in parts (b) and (d) represent the magnitudes of the magnetic moments normalized by $3.0\mu_B$ for the spin-up and spin-down states, respectively.

The effect of temperature on the formation of SRO has been investigated experimentally by electrical resistivity measurements [14,15] and theoretically using MC simulations with machine learning potentials [17,18]. Li *et al.* [14] reported that The SRO is present in the temperature range 673–973 K in CrCoNi, and the degree of SRO is higher at lower temperatures, but the kinetics of SRO are slower at lower temperatures. This result suggests that the SRO is energetically stable below 673 K in CrCoNi. The SRO in the temperature range 50–2000 K in CrCoNi was investigated using the MC simulations with machine learning potentials by Ghosh *et al.* [18]. They reported that the MoPt$_2$-type ordering occurred in the temperature range 180–975 K. On the other hand, Du *et al.* [17] reported that the SRO structure was formed below 800 K. To clarify the effect of temperature, we are performing more MC simulations at various temperatures in CrCoNi. Although the MC simulations have not yet reached the equilibrium state, the decrease in the potential energy suggesting the formation of SRO was observed below 900 K as shown in Fig. S2 in the Supplemental Material [29].

B. Average concentrations

To discuss the structure formed by SROs, the average concentrations of the various elements in the (100), (010), and (001) planes were examined. Figure 2 shows the change in the average concentration of each element in the (100), (010), and (001) planes during the MC simulations for CrCoNi and MnCoNi. It should be noted that if $L1_2$-type ordering occurs by SRO, a deviation in the average concentration should be observed in all {100} planes. During the MC simulations of up to 300 MC steps, the average concentrations of Cr in CrCoNi and Mn in MnCoNi deviated from 0.333 in all {100} planes, indicating that $L1_2$-type ordering took place. In $L1_2$-type ordering, Cr or Mn atoms preferentially occupy corner sites to avoid the formation of first NN bonds. However, in the case of equimolar ternary alloys, the face-centered sites are inevitably occupied by Cr or Mn atoms because the concentration of corner sites in the $L1_2$ structure is 0.25. If the occupation of face-centered sites is promoted in a particular direction, other types of SRO can begin to evolve after the initial stage. In the case of the MnCoNi alloy, the average concentration of Mn atoms in the (001) plane was found to steeply increase
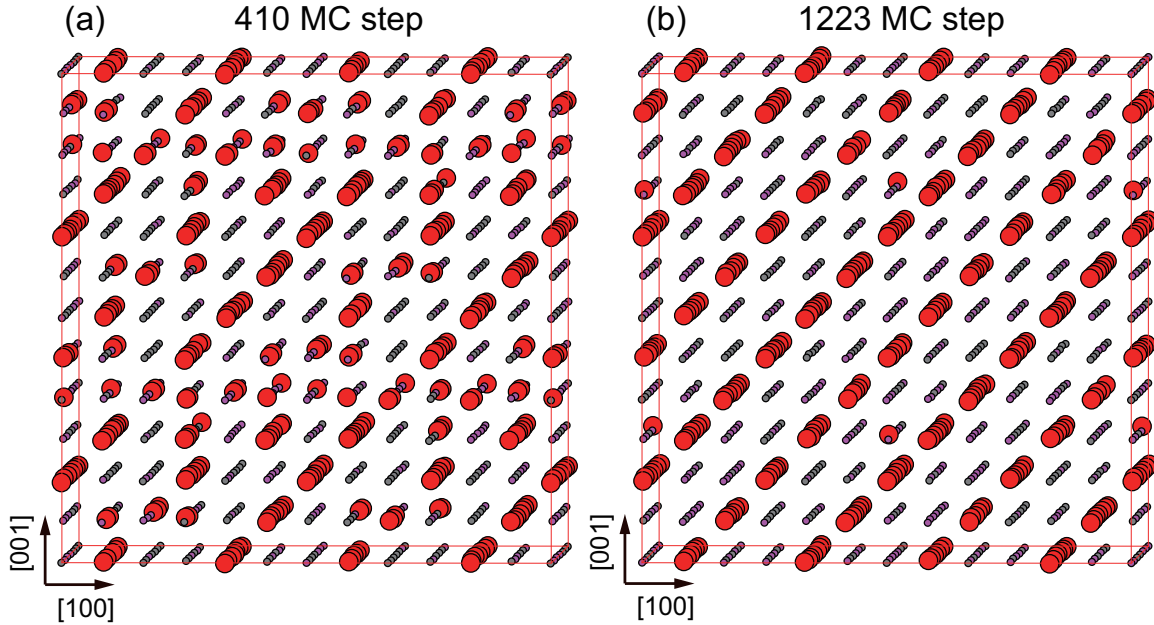
FIG. 5. Atomic arrangements of the Cr atoms in CrCoNi after (a) 410 and (b) 1223 MC steps.

after 300 MC steps. As a result, a maximum concentration of 0.667 was reached, leading to $L1_0$-type ordering wherein the Mn-rich and Mn-poor layers were alternately stacked along the [001] direction. It should be noted here that $L1_0$-type ordering in MnCoNi was recently confirmed by neutron scattering [20]. In contrast, in the case of CrCoNi, deviations in the average concentrations of Cr atoms were still observed in the (100) and (010) planes after the initial stage, although these gradually decreased after 400 MC steps. Although the SRO along the ⟨100⟩ direction was reduced after 400 MC steps, the WC parameters of the first NN pairs continued to exhibit large deviations from zero after 400 MC steps, with the exceptions of the Co-Co and Ni-Ni pairs, thereby suggesting that other types of SRO still exist.

C. Atomic and magnetic structures

In the $L1_0$-type ordering of MnCoNi, the Mn-rich and Mn-poor layers are alternately stacked along the [001] direction. Figure 3 shows the atomic and magnetic structures in the Mn-rich and Mn-poor layers of MoCoNi after 904 MC steps, in which the potential energy exhibited a minimum value. In the Mn-rich layer, all first NN Mn-Mn bonds formed antiparallel spin pairs. The Co clusters were found to be randomly distributed and exhibited parallel spin-up and spin-down states. As shown in Fig. 2(b), the concentration of Ni atoms in the Mn-rich layers was lower than that of Co atoms, and the Ni atoms mainly formed second NN Ni-Ni bonds with parallel spin states. In addition, the magnitude of the Ni spin was smaller than that of the Mn and Co atoms. In the Mn-poor layers, Co and Ni clusters were randomly distributed and exhibited parallel spin-up or spin-down states. Furthermore, the magnetic moments of the Co and Ni atoms in the Mn-poor layer were smaller than those of the Mn atoms. It should be considered that magnetic frustration in an fcc structure arises from the triangles formed by three first NN bonds, and so

the triangles are not located in the {100} planes but between adjacent {100} planes. As a result, the formation of Mn-rich and -poor alternating layers along the ⟨100⟩ direction led to a decrease in the magnetic frustration induced by the Mn-Mn parallel pairs.

Figure 4 shows the atomic and magnetic structures in the (100) and (010) planes of CrCoNi after 410 MC steps, where the WC parameter of the second Cr-Cr pair exhibited the minimum value. In the (100) plane, while a second NN Cr-Cr bond was formed, a first NN Cr-Cr bond was also observed. Unlike the first NN Mn-Mn bonds in MnCoNi, some of the first NN Cr-Cr bonds form parallel spin pairs. In the (010) plane, the Cr atoms were found to align along the [101] direction, and a similar trend was observed in the adjacent (010) planes. Moreover, all first NN Cr-Cr bonds formed antiparallel spin pairs in the (010) plane, suggesting that the Cr atoms preferentially occupy the (10$\bar{1}$) planes. To clarify the ordering of the Cr atoms, their atomic arrangements after 410 and 1223 MC steps were determined, as shown in Fig. 5. More specifically, after 410 MC steps, the Cr atoms preferentially occupied every six (10$\bar{1}$) planes, and Cr atoms were also located on the (100) and (001) planes. After 1223 MC steps, the number of Cr atoms located on the (100) and (001) planes decreased, and the (10$\bar{1}$) planes between the Cr-enriched (10$\bar{1}$) planes were occupied by Cr atoms. Consequently, all three (10$\bar{1}$) planes were preferentially occupied by Cr atoms. As shown in Fig. 1, the number of second NN Cr-Cr bonds reached a maximum after 410 MC steps and decreased with an increasing occupation of Cr atoms on the (10$\bar{1}$) planes. The changes in the average concentrations of the various elements over the six (10$\bar{1}$) planes of the supercell are shown in Fig. 6, wherein it can be seen that the corner sites of the $L1_2$ structure were located every two (10$\bar{1}$) planes. The occupation of Cr atoms on the (10$\bar{1}$) planes was therefore promoted every six layers from the initial stage of SRO, which was suppressed every six layers owing to competition with the $L1_2$-type ordering in the
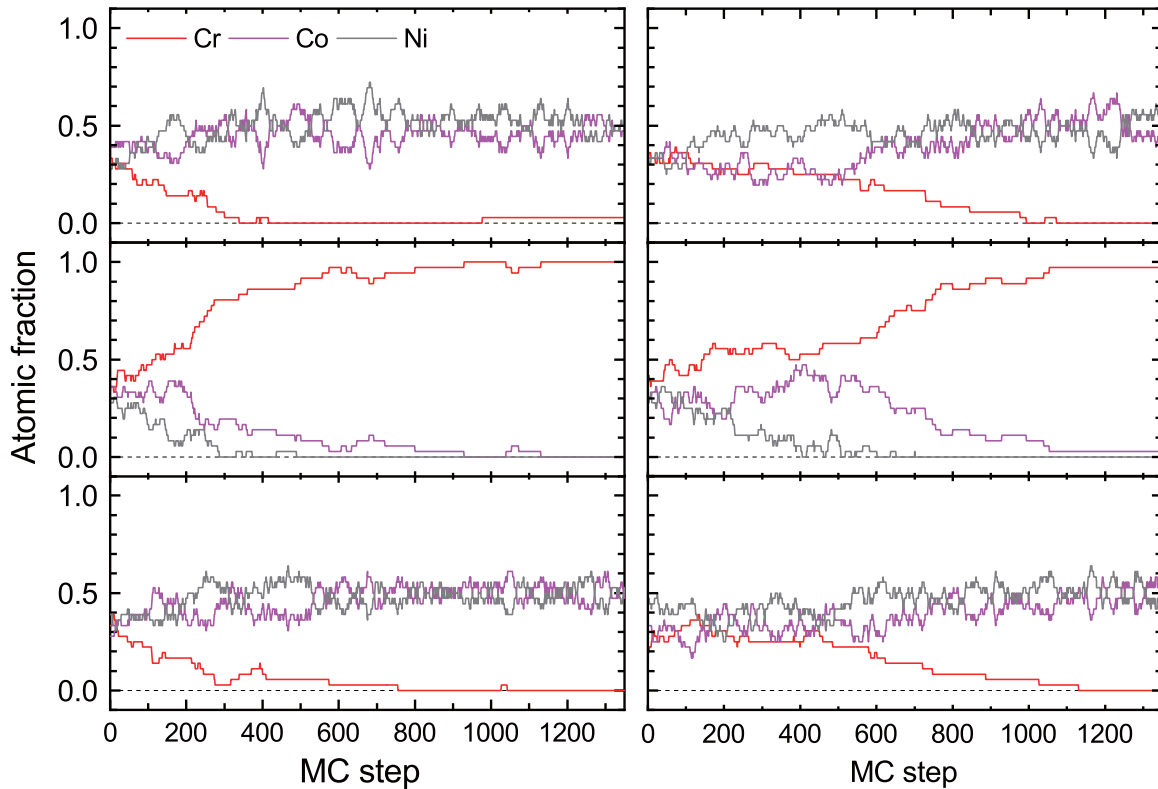
FIG. 6. Changes in the average concentrations of the various elements on the six $(10\bar{1})$ planes in the supercell during the MC simulation for CrCoNi.

initial stage. If every three {110} layers are perfectly occupied by Cr atoms, the WC parameters of the first and second NN Cr-Cr pairs become 0.5 and 0.0, respectively, which agrees with the WC parameters observed in the MC simulations for CrCoNi. The Co and Ni atoms were almost equally distributed in the other $(10\bar{1})$ planes. Furthermore, Fig. 7 shows the atomic and magnetic structures in the Cr-rich $(10\bar{1})$ plane of CrCoNi after 1223 MC steps. It can be seen that the first NN Cr-Cr bonds, with the exception of those around the Co atom, were antiparallel pairs in the Cr-rich $(10\bar{1})$ planes. Moreover, the magnitude of the magnetic moment in the Cr-rich $(10\bar{1})$ plane of CrCoNi was smaller than that in the Mn-rich (001) plane of MnCoNi.

In addition to the {100} superlattice, the {110} superlattice with an alternating arrangement of {110} Cr-rich and Co/Ni-rich layers was reported by Du *et al.* based on a large-scale MC simulation with a neural network potential [17]. The energy difference between the {100} and {110} superlattices was investigated using 108-atom supercells and it was concluded that the average enthalpy difference between the two superlattices was only 0.027 eV/atom. In the current study, the Cr-rich (100), (001), and $(10\bar{1})$ planes coexisted after 410 MC steps, and the Cr-rich (100) and (001) planes almost disappeared after 1223 MC steps. The energy gain after 410 MC steps was 0.019 eV/atom, which is in reasonable agreement with the results of a previous study. The {110} superlattice was also confirmed using machine learning potentials by Ghosh *et al.* [18]. They have identified the {110} superlattice as the MoPt$_2$-type ordering. The alignment of magnetic moments of the MoPt$_2$-type ordering was deter-

mined using 108-atom supercells and it was found that Co atoms are aligned ferromagnetically and Cr atoms reveal an antiparallel magnetic moment with neighboring Cr and Co atoms. However, some of the Cr atoms have zero magnetic moment and the antiferromagnetic alignment of the first NN Cr-Cr pairs is not well reproduced. This may be because the atomic arrangement of Co and Ni-rich layers in the supercell does not sufficiently reproduce the atomic arrangement of the SRO. The antiferromagnetic alignment of Cr atoms located in $(10\bar{1})$ planes is the same magnetic ordering that has been predicted for the Cr sublattice in CrNi$_2$ [30].

The Cr-rich $(10\bar{1})$ plane of CrCoNi shown in Fig. 5(b) was formed across the supercell boundary, which suggests that larger supercells are necessary to estimate the domain size of the MoPt$_2$-type ordering. While it is difficult to employ larger supercells in first-principles-based Monte Carlo simulations, the average domain size obtained by the Monte Carlo simulations using a 2916-atom supercell with machine learning potentials is about 6 Å at temperatures above 800 K [17].

As mentioned above, Inoue *et al.* reported the modulation from a random distribution along the [001] direction in CrCoNi using atom probe tomography [10]. In contrast, Zhou *et al.* proposed the alternating Cr-enriched and Co/Ni-enriched {113} planes in CrCoNi based on observations using aberration-corrected transmission electron microscopy [11]. Since the lattice sites on every two {113} planes coincide with those on every four {110} planes in the fcc structure, the stacking sequence of the Cr-enriched planes does not agree with that in the MoPt$_2$-type ordering. Every three {110} planes occupied by Cr atoms in the MoPt$_2$-type ordering,
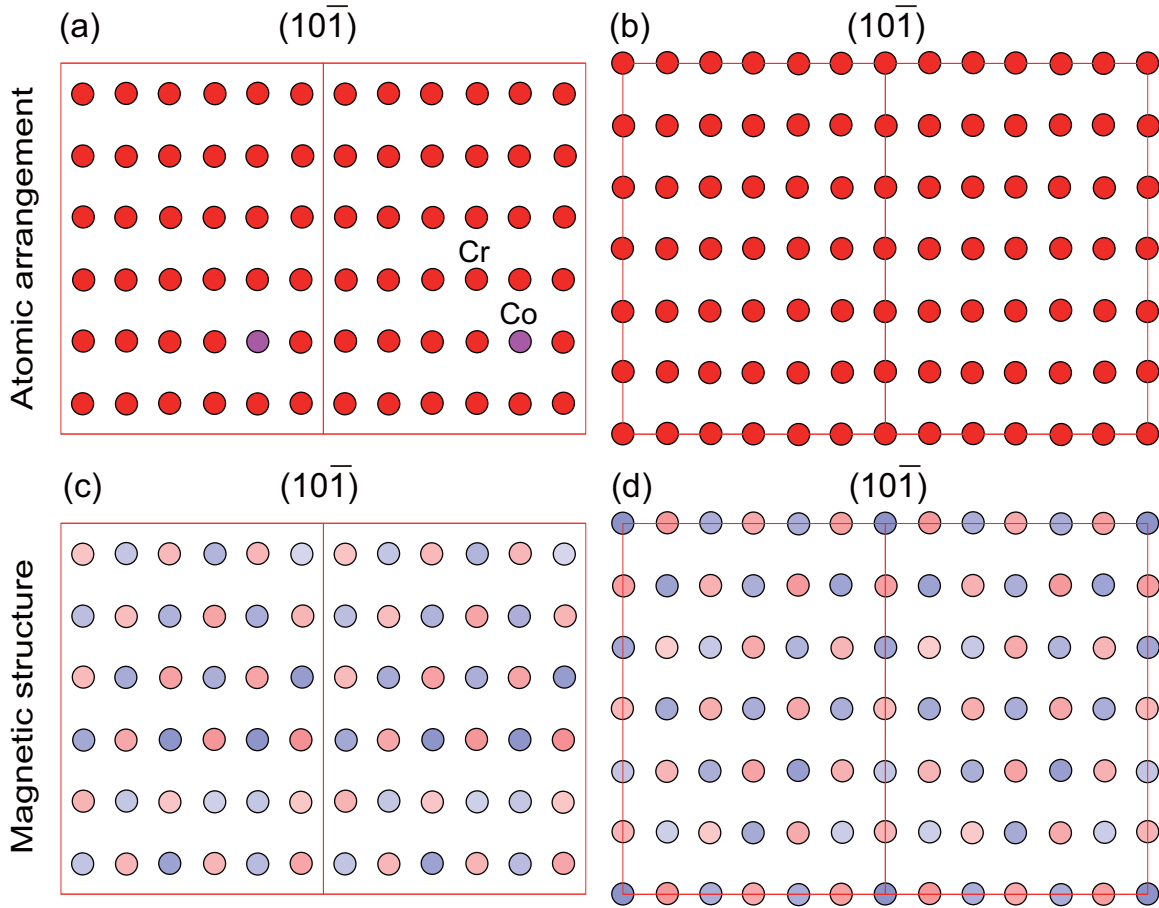
FIG. 7. (a), (c) Atomic and (b), (d) magnetic structures in the Cr-rich $(10\bar{1})$ planes in CrCoNi after 1223 MC steps. The red and blue shadings in parts (b) and (d) represent the magnitudes of the magnetic moments normalized by $3.0\mu_{\rm B}$ for the spin-up and spin-down states, respectively.

which is consistent with the atomic fraction of Cr atoms in CrCoNi. Although the MoPt$_2$-type ordering of Cr atoms in the SRO of CrCoNi has been supported by recent theoretical works [4,17,18], further studies are still needed to clarify the structure of the Cr/CoNi {110} superlattice. The detail of the relationship between {110} and {113} planes was provided in the Supplemental Material [29].

D. Magnetic moments

Figure 8 shows the changes in the average magnetic moments in the two alloys during the MC simulations. More specifically, the average magnetic moment of the Cr atoms in CrCoNi increased for up to 400 MC steps and then decreased continuously, whereas the other atoms exhibited gradual changes during the MC simulations. As discussed below, the increase and decrease in the average magnetic moment of the Cr atoms in CrCoNi originate from the decrease in the minority-spin and majority-spin density of states (DOS) near the Fermi level, respectively. Compared to the magnetic moment in CrCoNi, the Mn, Co, and Ni atoms in MnCoNi were found to possess larger magnetic moments. The change in the magnetic moment during the MC simulation was not significant, with the exception of a slight increase

observed for the Mn atoms in the initial stage of the SRO. Furthermore, Fig. 9 shows the change in the sum of the products of the magnetic moments of all bonds in the supercells during the MC simulations of CrCoNi and MnCoNi. In MnCoNi, the number of parallel pairs of Mn-Mn bonds decreased during the MC simulations, which suggests that the SRO mainly originates from the decrease in the magnetic frustration of Mn-Mn bonds. Although the Cr-Cr bonds in CrCoNi show a similar trend, the product of the magnetic moments of the Cr-Cr bonds is significantly smaller than that of the Mn-Mn bonds. Instead, the antiparallel pairs of Co-Co bonds in CrCoNi showed a steep decrease in the initial MC steps.

The magnetic properties have systematically been investigated in Ni-based equiatomic fcc alloys by Jin *et al.* [31] and in fcc Cr$_x$CoNi alloys by Sales *et al.* [32]. The authors concluded that CrCoNi was paramagnetic above 5 K. Therefore, the magnetic state of CrCoNi is paramagnetic at 300 K. Although, to simulate the paramagnetic state, the up and down spins were distributed using the binary SQS model for the initial magnetic moment; the antiferromagnetic order appears as shown in Fig. 7 during the MC simulation due to the lack of finite-temperature effects [33]. To evaluate the energy gain by the antiferromagnetic alignment, the
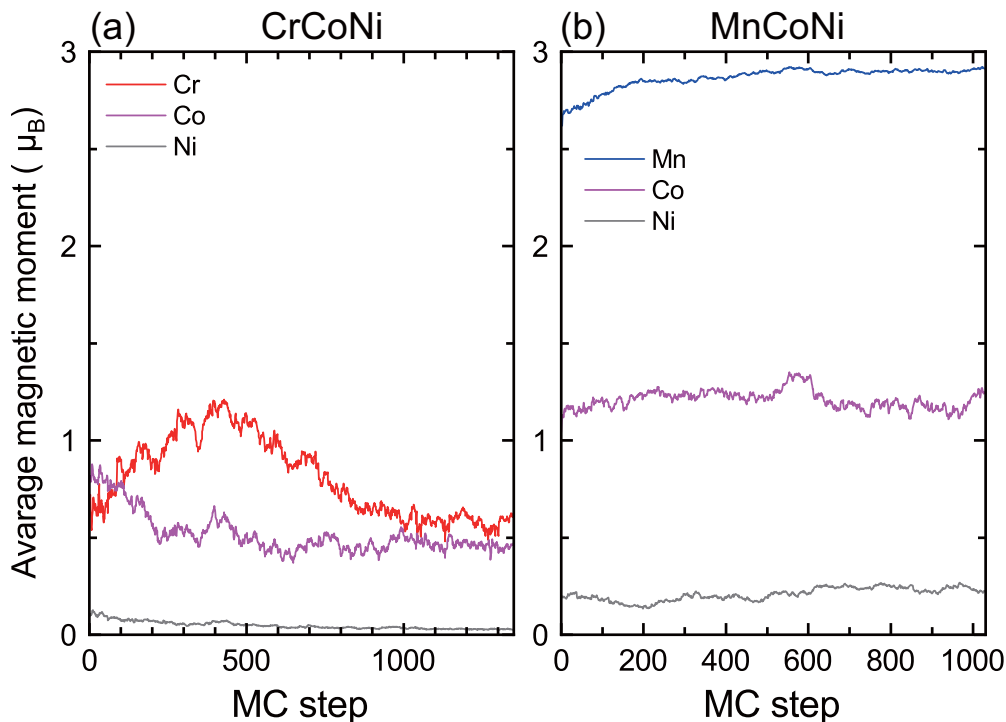
FIG. 8. Changes in the average magnetic moments of the various elements during the MC simulations for (a) CrCoNi and (b) MnCoNi.

potential energies after 410 and 1223 MC steps were obtained by non-spin-polarized calculations. The energy gain by the antiferromagnetic alignment after 410 and 1223 MC steps was 0.0067 and 0.0023 eV/atom, respectively. The difference in the energy gain arises from the decrease in the

magnetic moment observed after 410 MC steps in CrCoNi. Therefore, compared with $L1_2$-type ordering formed in the initial stage, the contribution by the antiferromagnetic alignment to the occupation of Cr atoms on the {110} planes is small.
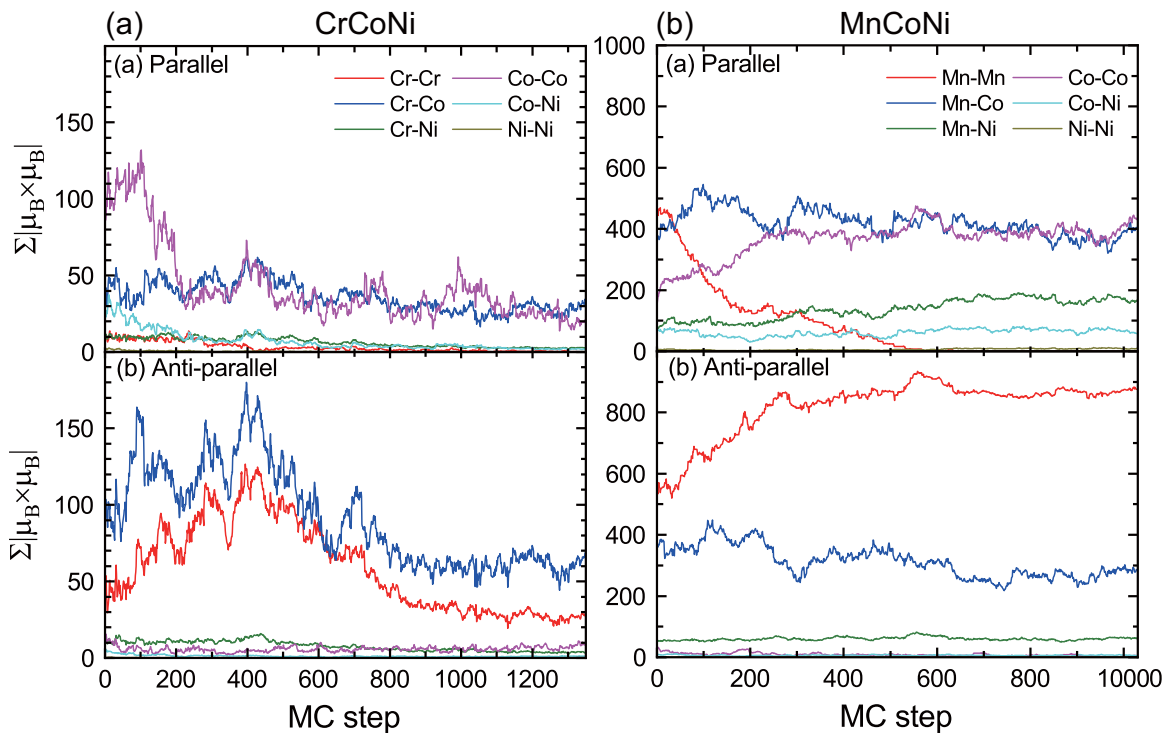

FIG. 9. Changes in the sums of the products of the magnetic moments of all bonds in the supercells during the MC simulations for (a) CrCoNi and (b) MnCoNi.
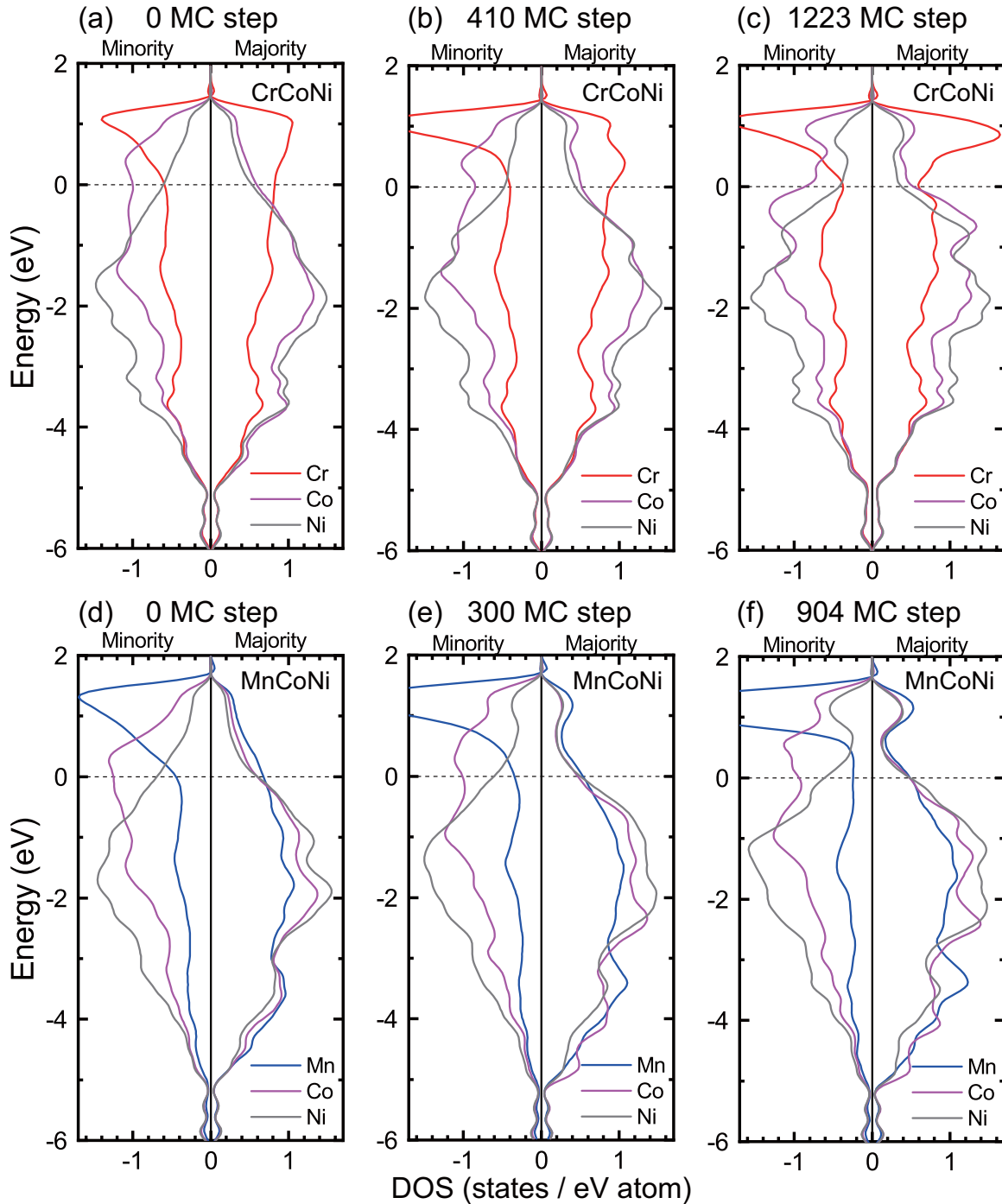
FIG. 10. Average partial DOS for each element (a) before the MC simulation (0 MC steps), (b) after 410 MC steps, and (c) after 1223 MC steps for CrCoNi, along with those (d) before the MC simulation (0 MC steps), (e) after 300 MC steps, and (f) after 904 MC steps for MnCoNi.

IV. DISCUSSION

To clarify the origin of the SRO, changes in the DOS induced by the SRO were examined. Figure 10 shows the average partial DOS for each element in CrCoNi and MnCoNi before and after the MC simulations. A common feature observed for each element was a decrease in the DOS near the Fermi level, which led to an energy gain induced by the SRO. This can be attributed to the fact that the DOS near the Fermi level is primarily composed of antibonding states. As

shown in Fig. 1, the most pronounced change around the Cr atoms was a decrease in the number of the first NN Cr-Cr bonds, which reduced the magnetic frustration of the Cr-Cr parallel pairs. After 410 MC steps, the minority-spin DOS near the Fermi level of the Cr atoms decreased in CrCoNi compared to that before the MC simulation. This change in the WC parameters indicated that the number of first NN Cr-Cr pairs decreased, reducing the magnetic frustration induced by the parallel-spin pairs, and leading to a decrease in the minority-spin DOS near the Fermi level. Therefore, the

magnetic moments of the Cr atoms increased during the MC simulation. However, after 1223 MC steps, a decrease in the DOS was observed around the Fermi level in the majority-spin band of the Cr atoms. It should be noted here that in equimolar ternary solid-solution alloys with an fcc structure, the average number of neighboring Cr atoms is 4. As shown in Fig. 6, the occupation of Cr atoms on the $(10\bar{1})$ planes progressed after 410 MC steps. If the Cr atoms occupy every three $(10\bar{1})$ planes, the first NN Cr-Cr bonds exist only in the $(10\bar{1})$ plane, and the average number of neighboring Cr atoms becomes 2. Therefore, the number of first NN Cr-Cr pairs continued to decrease after 410 MC steps. In contrast, the number of first NN Cr-Co and Cr-Ni pairs increased, leading to a decrease in the majority-spin DOS of the Cr atoms near the Fermi level. Therefore, the magnetic moment of the Cr atoms decreased after 410 MC steps. A decrease in the DOS near the Fermi level was also observed in the minority spin band of the Co atoms and in the majority and minority bands of the Ni atoms during the MC simulation, which contributed to the energy gain by SRO. Similar decreases in the DOS of the Co and Ni atoms in MnCoNi were observed during the MC simulation. Comparing the DOS of the Mn atoms in MnCoNi and that of the Cr atoms in CrCoNi, it was clear that the Mn atoms exhibit a larger difference between the majority- and minority-spin DOS, which gives rise to larger magnetic moments for the Mn atoms.

To clarify the change in the DOS of the SRO, the magnetic quantum number-resolved DOS was examined. Thus, Fig. 11 shows the average partial DOS for each $3d$ orbital of the Cr atoms in CrCoNi and of the Mn atoms in MnCoNi both before and after the MC simulations. In an ideal fcc solid solution, the $3d$ orbitals are split into two groups; one consists of the $3d_{xy}$, $3d_{yz}$, and $3d_{zx}$ orbitals, which are known as the t_{2g} orbitals, while the other consists of the $3d_{x^2-y^2}$ and $3d_{z^2}$ orbitals, which are known as the e_g orbitals. It was possible to split the $3d$ orbitals of the CrCoNi and MnCoNi alloys into these two groups before the MC simulations, indicating that the SQS models employed in this study can accurately reproduce the electronic structures of ideal solid solutions. The splitting of the $3d$ orbitals can be used to determine the type of SRO. In addition, if $L1_2$-type ordering occurs by SRO, no further splitting is observed, and the occupation of the face-centered sites by Cr or Mn atoms randomly occurs in the {100} planes. If the face-centered sites in one of the {100} planes are preferentially occupied, further splitting of the DOS takes place due to a lowering of the symmetry. In the case of the MnCoNi alloy, although the shape of the DOS slightly changed after 300 MC steps, no further DOS splitting was observed. Therefore, $L1_2$-type ordering was still observed after 300 MC steps. After 904 MC steps, in which the Mn-rich and Mn-poor layers were alternately formed along the (001) direction by $L1_0$-type ordering (see Fig. 2), the $3d_{xy}$ orbital was split from the $3d_{yz}$ and $3d_{zx}$ orbitals in the majority-spin DOS, and as a result, a decrease at around the Fermi level and an increase at approximately -1.5 eV was observed. The $3d_{z^2}$ orbitals exhibited similar changes, leading to an energy gain through $L1_0$-type ordering. However, in the case of the CrCoNi alloy, the WC parameter of the second NN Cr-Cr pair exhibited a minimum value after 410 steps, and further splitting was observed near the Fermi level in the

majority-spin DOS. This was due to the occurrence of both $L1_2$-type ordering and the occupation of Cr atoms on the $(10\bar{1})$ planes. After 1223 MC steps, an increase in the DOS of the $3d_{zx}$ orbital was observed at -1.3 eV in the majority- and minority-spin DOS, which originated from the formation of first NN Cr-Cr pairs along the [101] direction in the $(10\bar{1})$ planes.

The most pronounced difference in the DOS between the CrCoNi and MnCoNi alloys was the magnitude of the spin polarization, which led to differences between the majority- and minority-spin DOS. Although the contribution of the minority-spin band of the Mn atoms is particularly small in MnCoNi, the shape and size of the minority-spin band of the Cr atoms was similar to the majority-spin band below -1.0 eV in CrCoNi. As a result, the minority-spin band of the $3d$-t_{2g} orbitals of the Cr atoms played an important role in the formation of the {110} superlattice by SRO. Thus, to clarify the role of the Cr atoms in SRO, MC simulations were performed for CrFeCoNi and CrMnFeCoNi. Although the change in energy induced by SRO did not converge, a difference in the DOS of the Cr atoms was observed. Figure 12 shows the average partial DOS of the Cr atoms in the CrCoNi, CrFeCoNi, and CrMnFeCoNi alloys after the MC simulations, in which the energy gain reached 0.06 eV/atom. More specifically, for both CrFeCoNi and CrMnFeCoNi, the spin polarization was enhanced by SRO, and the shape of the majority-spin band of the Cr atoms was similar to that of the Mn atoms in MnCoNi. In addition, the occupation of the {110} planes by Cr atoms was not observed for the CrFeCoNi and CrMnFeCoNi alloys. These results suggest that a decrease in the spin polarization of the Cr atoms determines the type of SRO in Cr-containing fcc concentrated solid-solution alloys. There are two possible reasons for the smaller spin polarization of the Cr atoms in CrCoNi. First, Mn or Fe atoms, which induce spin polarization of the Cr atoms, are not present in CrCoNi. In CrMnFeCoNi, the Cr atoms exhibited large spin polarization in the Cr-Mn and Cr-Fe pairs. Second, the Cr concentration of CrCoNi was higher than those of CrFeCoNi and CrMnFeCoNi. In future studies, the effect of the Cr concentration on the SRO in CrCoNi will be investigated. It is expected that if a lower Cr concentration induces spin polarization of the Cr atoms, CrCoNi alloys could exhibit larger spin polarization of the Cr atoms, and $L1_0$-type ordering could be observed upon reducing the Cr concentration.

V. SUMMARY

Due to the magnetic frustration of parallel spin pairs in Cr- or Mn-containing face-centered-cubic (fcc) concentrated solid-solution alloys, short-range order (SRO) is expected. Thus, in the current study, the SRO in fcc CrCoNi and MnCoNi medium-entropy alloys was investigated using first-principles-based Monte Carlo (MC) simulations. It was found that in the initial stage of the SRO, the first and second nearest neighbor (NN) Cr-Cr bonds in the CrCoNi alloy were found to decrease and increase, respectively. A similar trend was observed for the Mn-Mn bonds in MnCoNi. These changes led to $L1_2$-type ordering, which originates from the energy gain owing to the decrease in the magnetic frustration of
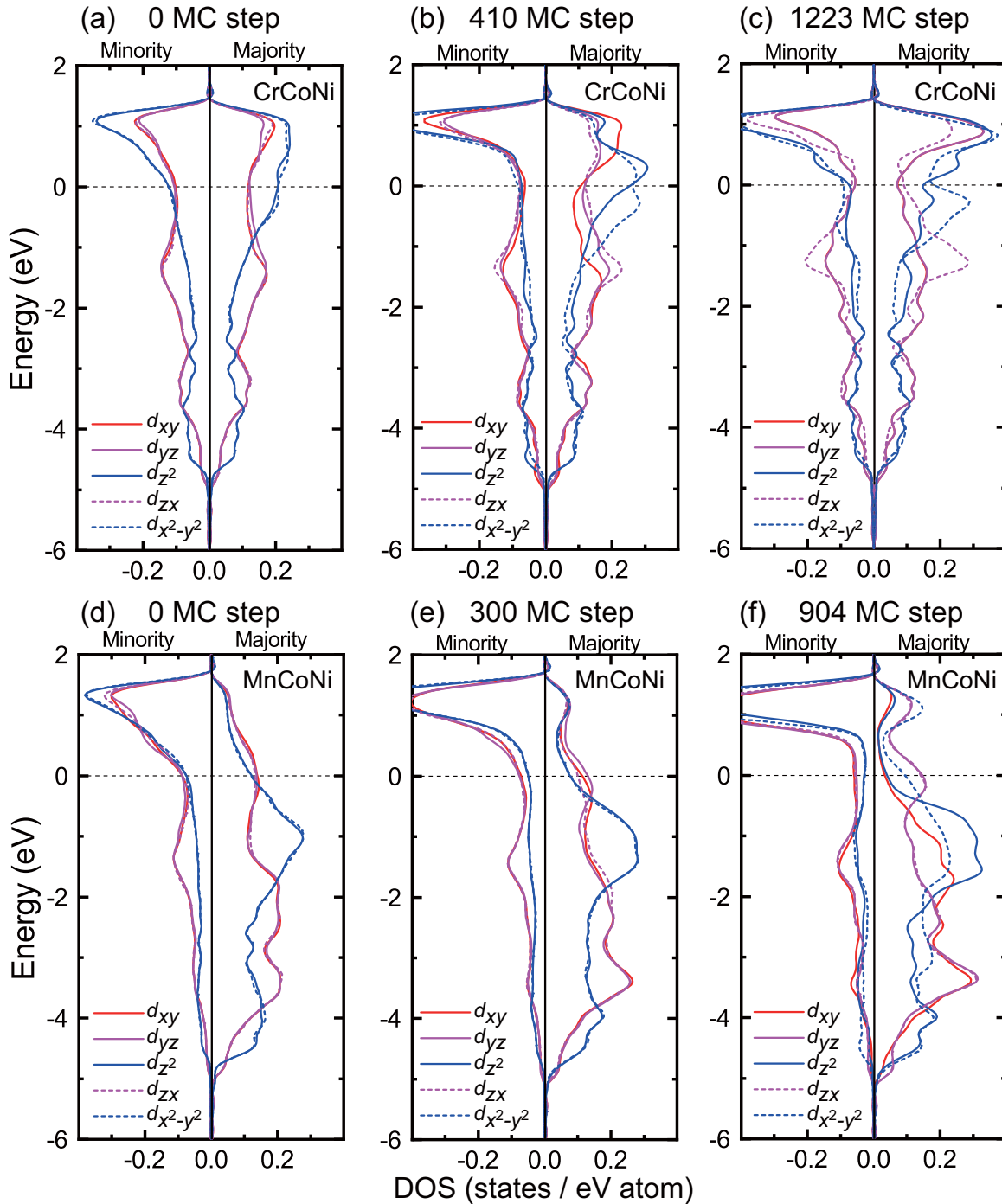
FIG. 11. Average partial DOS for each $3d$-orbital of the Cr atoms (a) before the MC simulation (0 MC steps) [34], (b) after 410 MC steps, and (c) after 1223 MC steps for CrCoNi, along with those of the Mn atoms (d) before the MC simulation (0 MC steps), (e) after 300 MC steps, and (f) after 904 MC steps for MnCoNi.

the Cr-Cr or Mn-Mn parallel pairs. In the case of equimolar ternary alloys, Cr-Cr or Mn-Mn parallel pairs were inevitably formed by $L1_2$-type ordering because the concentration of corner sites in the $L1_2$ structure is 0.25. Therefore, other types of SRO began to evolve after this initial stage. After the initial stage, it was found that the change in the Mn concentration progressed along one of the $\langle 100 \rangle$ directions in MnCoNi. This led to $L1_0$-type ordering, wherein the Mn-rich

and Mn-poor planes were stacked alternately along one of the $\langle 100 \rangle$ directions. In the Mn-rich layers, antiparallel Mn-Mn pairs were formed, while clusters of Ni and Co atoms were distributed throughout the Mn-poor layers. The formation of Mn-rich and Mn-poor layers in the $L1_0$-type ordering led to a decrease in the number of Mn-Mn parallel pairs between the {100} layers. However, the occupation of Cr atoms on one of the {110} planes in CrCoNi began to increase steeply
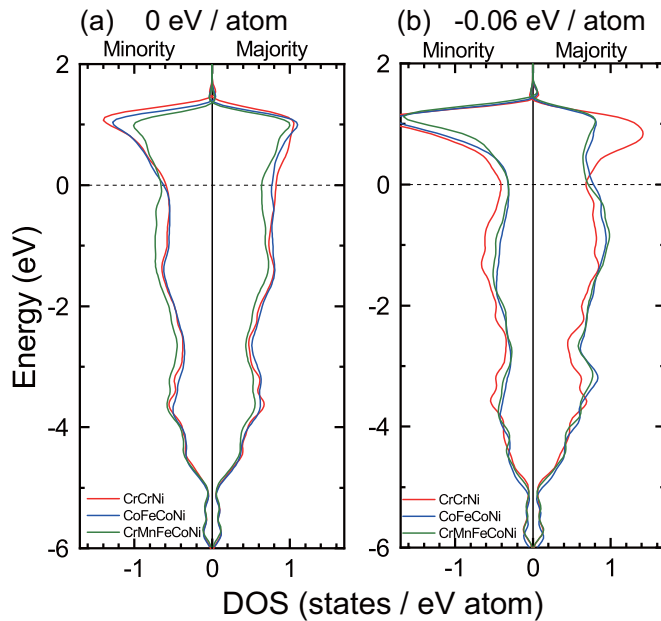
FIG. 12. Average partial DOS for the Cr atoms in CrCoNi, CrFeCoNi, and CrMnFeCoNi (a) before the MC simulations and (b) after the MC simulations in which the energy gain reached 0.06 eV/atom.

after the initial stage. Although the occupation of Cr atoms on the {110} planes increased every three layers, the occupation of Cr atoms on the {110} planes was suppressed every six layers. This was due to the competition with the $L1_2$-type ordering in the initial stage. With an increasing occupation of the {110} planes by the Cr atoms, the number of second NN Cr-Cr bonds decreased, and antiparallel Cr-Cr pairs were formed in the Cr-rich {110} planes. The key difference in the SRO observed after the initial stage for the CrCoNi and MnCoNi alloys was induced by the different magnetic moments of the Cr and Mn atoms: The Cr atoms in Cr-CoNi possess the lower magnetic moment compared with the of Mn atoms in MnCoNi. Although the majority-spin band of the Mn atoms contributes to the formation of antiparallel pairs in the $L1_0$-type ordering, both the majority- and minority-spin bands of the 3d t_{2g} orbitals play an important role in the formation of the {110} superlattice referred to as $MoPt_2$-type ordering in CrCoNi. The energy gain due to the formation of SRO in MnCoNi was determined to be approximately twice that in CrCoNi, suggesting that MnCoNi possesses a larger driving force for the formation of SRO than CrCoNi.

ACKNOWLEDGMENT

[1] A. Tamma, A. Aabloo, M. Klintenberg, M. Stocks, and A. Caro, Acta Mater. **99**, 307 (2015).

[2] C. Niu, A. J. Zaddach, A. A. Oni, X. Sang, J. W. Hurt, J. M. LeBeau, C. C. Koch, and D. L. Irving, Appl. Phys. Lett. **106**, 161906 (2015).

[3] F. Walsh, M. Astaa, and R. O. Ritchie, Proc. Natl. Acad. Sci. USA **118**, e2020540118 (2021).

[4] C. D. Woodgate, D. Hedlund, L. H. Lewis, and J. B. Staunton, Phys. Rev. Mater. **7**, 053801 (2023).

[5] B. Cantor, I. T. H. Chang, P. Knight, and A. J. B. Vincent, Mater. Sci. Eng. A **375–377**, 213 (2004).

[6] M. Mizuno, K. Sugita, and H. Araki, Compt. Mater. Sci. **170**, 109163 (2019).

[7] F. X. Zhang, S. Zhao, K. Jin, H. Xue, G. Velisa, H. Bei, R. Huang, J. Y. P. Ko, D. C. Pagan, J. C. Neuefeind, W. J. Weber, and Y. Zhang, Phys. Rev. Lett. **118**, 205501 (2017).

[8] R. Zhang, S. Zhao, J. Ding, Y. Chong, T. Jia, C. Ophus, M. Asta, R. O. Ritchie, and A. M. Minor, Nature (London) **581**, 283 (2020).

[9] B. Yin, S. Yoshida, N. Tsuji, and W. A. Curtin, Nat. Commun. **11**, 2507 (2020).

[10] K. Inoue, S. Yoshida, and N. Tsuji, Phys. Rev. Mater. **5**, 085007 (2021).

[11] L. Zhou, Q. Wang, J. Wang, X. Chen, P. Jiang, H. Zhou, F. Yuan, X. Wu, Z. Cheng, and En. Ma, Acta Mater. **224**, 117490 (2022).

[12] H. W. Hsiao, R. Feng, H. Ni, K. An, J. D. Poplawsky, P. K. Liaw, and J. M. Zuo, Nat. Commun. **13**, 6651 (2022).

[13] G. Tang, Z. Zhang, Y. Liu, Y. Wang, X. Wu, and X. Liu, Mater. Des. **225**, 111572 (2023).

[14] L. Li, Z. Chen, S. Kuroiwa, M. Ito, K. Yuge, K. Kishida, H. Tanimoto, Y. Yu, H. Inui, and E. P. George, Acta Mater. **243**, 118537 (2023).

[15] T. Teramoto, K. Kitasumi, R. Shimohara, Y. Ito, R. Shimizu, K. Tanaka, and R. Ueji, J. Alloys Compd. **941**, 169016 (2023).

[16] J. Ding, Q. Yu, M. Asta, and R. O. Ritchie, Proc. Natl. Acad. Sci. USA **115**, 8919 (2018).

[17] J. P. Du, P. Yu, S. Shinzato, F. S. Meng, Y. Sato, Y. Li, Y. Fan, and S. Ogata, Acta Mater. **240**, 118314 (2022).

[18] S. Ghosh, V. Sotskov, A. V. Shapeev, J. Neugebauer, and F. Körmann, Phys. Rev. Mater. **6**, 113804 (2022).

[19] J. Cowley, Phys. Rev. **77**, 669 (1950).

[20] Y. Umenoto, Y. Ikeda, and M. Fujita, Mater. Trans. **64**, 2018 (2023).

[21] M. Mizuno, K. Sugita, and H. Araki, Results Phys. **34**, 105285 (2022).

[22] A. Zunger, S.-H. Wei, L. G. Ferreira, and J. E. Bernard, Phys. Rev. Lett. **65**, 353 (1990).

[23] W. K. Hasting, Biometrica **57**, 97 (1970).

[24] G. Kresse and J. Hafner, Phys. Rev. B **47**, 558 (1993).

[25] G. Kresse and J. Furthmüller, Phys. Rev. B **54**, 11169 (1996).

[26] J. P. Perdew, K. Burke, and M. Ernzerhof, Phys. Rev. Lett. **77**, 3865 (1996).

[27] P. E. Blöchl, Phys. Rev. B **50**, 17953 (1994).

[28] G. Kresse and D. Joubert, Phys. Rev. B **59**, 1758 (1999).

[29] See Supplemental Material at http://link.aps.org/supplemental/10.1103/PhysRevMaterials.8.013601 for the evaluations of kinetic energy cutoff and k mesh, the details of the change in the potential energy, the MC simulations at various temperatures in CrCoNi, and the relationship between {110} and {113} planes.

[30] F. Walsh, R. O. Ritchie, and M. Asta, Phys. Rev. Mater. **6**, 113602 (2022).

[31] K. Jin, B. C. Sales, G. M. Stocks, G. D. Samolyuk, M. Daene, W. J. Weber, Y. Zhang, and H. Bei, Sci. Rep. **6**, 20159 (2016).

[32] B. C. Sales, K. Jin, H. Bei, G. M. Stocks, G. D. Samolyuk, A. F. May, and M. A. McGuire, Sci. Rep. **6**, 26179 (2016).

[33] F. Moitzi, L. Romaner, A. V. Ruban, and O. E. Peil, Phys. Rev. Mater. **6**, 103602 (2022).

[34] M. Mizuno and H. Araki, J. Jpn. Soc. Cryst. **65**, 183 (2023).